RESEARCH ARTICLE

NANO · MICRO small
www.small-journal.com

Extending Cycling Life Beyond 300 000 Cycles in Aqueous Zinc Ion Capacitors Through Additive Interface Engineering

Wenchao Shi, Zhenjun Song, Weiyi Sun, Yu Liu, Yalong Jiang, Qi Li, and Qinyou An**

Developing low-cost and long-cycling-life aqueous zinc (Zn) ion capacitors (AZICs) for large-scale electrochemical energy storage still faces the challenges of dendritic Zn deposition and interfacial side reactions. Here, an interface engineering strategy utilizing a dibenzenesulfonimide (BBI) additive is employed to enhance the stability of the Zn metal anode/electrolyte interface. The first-principles calculation results demonstrate that BBI anions can be chemically adsorbed on Zn metal. Meanwhile, the experimental results confirm that the BBI-Zn interfacial layer converts the original water-richelectric double layer (EDL) into a water-poor EDL, effectively inhibiting the water related parasitic reaction at the electrode/electrolyte interface. In addition, the BBI-Zn interfacial layer introduces an additional Zn ions (Zn^{2+}) migration energy barrier, increasing the Zn^{2+} de-solvation activation energy, consequently raising the Zn^{2+} nucleation overpotential, and thus achieving the compact and uniform Zn deposition behavior. Furthermore, the solid electrolyte interphase (SEI) layer derived from the BBI-Zn interfacial layer during cycling can further maintain the interfacial stability of the Zn anode. Owing to the above favorable features, the assembled AZIC exhibits an ultra-long cycling life of over 300 000 cycles based on the additive engineering strategy, which shows application prospects in high-performance AZICs.

1. Introduction

Driven by the rapid advancement of renewable energy and the growing global demand for electricity, large-scale electrochemical energy storage (EES) systems become crucial for achieving a sustainable energy supply.[1] Seeking low-cost, long-cycling-life EES devices is the main challenge currently.[2] Aqueous zinc (Zn) ion capacitors (ZICs), as emerging EES devices, are considered one of the most attractive candidates for EES due to their advantages of high energy and power density, abundant resource of zinc, and low-cost aqueous electrolytes.[3]

However, AZICs also face similar challenges with aqueous Zn ion batteries (AZIBs) due to zinc anodes, including the Zn dendrites, hydrogen evolution reaction (HER), and corrosion reaction.[4] In addition, these interfacial issues may be more challenging under the high-frequency and high-current operation of the device.[5] Nevertheless, various interface stabilization strategies developed for AZIBs can offer valuable insights for AZICs as well. These strategies include Zn metal structure design,[6] separator modification,[7] high-concentration salt electrolytes,[8] surface coatings,[9] and electrolyte additives,[10] etc. Among them, additive interface engineering has recently attracted significant attention due to its cost-effectiveness, simple operation, broad application prospects, and significant improvement of interfacial stability.[10] For example, Liu et al. reported that the addition of glycine achieved uniform Zn deposition by adjusting the solvation shell structure of Zn ion (Zn^{2+}).[11] Huang et al. incorporated saccharin into the electrolyte, leading to a remarkable improvement in the interfacial stability of the Zn anode, by altering the electric double layer (EDL) structure and generating a solid electrolyte interphase (SEI) on the Zn anode.[12] Indeed, even trace amounts of electrolyte additives can bring about significant modifications to both the electrode/electrolyte interface structure and the electrochemical behavior of the Zn anode. However, to date, the regulation mechanism of additives on improving electrode/electrolyte interfacial stability is still controversial, and the application of additives to dendrite-free AZICs with long cycling life has been rarely explored.

Herein, a brightening agent, dibenzenesulfonimide (BBI) was introduced into the aqueous $ZnSO_4$ electrolyte to improve the

W. Shi, W. Sun, Y. Liu, Q. An
State Key Laboratory of Advanced Technology for Materials Synthesis and Processing
Wuhan University of Technology
Wuhan 430070, P. R. China
E-mail: anqinyou86@whut.edu.cn

Z. Song
School of Pharmaceutical and Materials Engineering
Taizhou University
Taizhou 318000, P. R. China

Y. Jiang
State Key Laboratory of New Textile Materials and Advanced Processing Technologies
Wuhan Textile University
Wuhan 430200, P. R. China

Q. Li
National Energy Key Laboratory for New Hydrogen-Ammonia Energy Technologies
Foshan Xianhu Laboratory
Foshan 528200, P. R. China
E-mail: liqi1@xhlab.cn

The ORCID identification number(s) for the author(s) of this article can be found under https://doi.org/10.1002/smll.202308282

DOI: 10.1002/smll.202308282

interfacial stability of the Zn anode. The theoretical calculation results indicated that BBI anions have strong chemical absorption interaction with Zn metal. Additionally, the experimental results confirmed the formation of a BBI-Zn interfacial layer on Zn metal, which reconstructed a water-poor EDL at the electrode/electrolyte interface, effectively suppressing HER and corrosive side reactions. Moreover, this interfacial layer regulated the migration behavior and de-solvation process of Zn^{2+}, increasing the nucleation overpotential,and thus resulting in a compact and uniform Zn deposition. Furthermore, the SEI derived from the BBI-Zn interfacial layer further maintained the interfacial stability. Based on the BBI's interface regulation of zinc anode, our assembled Zn||Zn symmetric cell demonstrated a cycling life of over 800 h at 10 mA cm^{-2} and 5 mAh cm^{-2}, far exceeding the $ZnSO_4$ electrolyte. In addition, its cycling life can reach 5,000 h at 1 mA cm^{-2}, demonstrating extremely superior cycling stability. Moreover, our assembled coin-type AZIC exhibited exceptional durability, beyond 300 000 cycles at 10 A g^{-1}, equivalent to a cumulative duration of over six months. Additionally, the assembled pouch AZIC can maintain a capacity retention of 80% after 6000 cycles, demonstrating its significant potential for practical applications.

2. Results and Discussion

Figure 1a,b illustrates the Zn deposition behavior in two electrolytes, respectively. In the case of the $ZnSO_4$ electrolyte, the Zn deposition layer exhibited a loose and porous morphology. However, when using the BBI/$ZnSO_4$ electrolyte, the Zn deposition layer showed a compact and uniform morphology, effectively preventing the formation of Zn dendrites. Scanning electron microscopy (SEM) images confirmed the different Zn deposition behavior under 10 mA cm^{-2} and 5 mAh cm^{-2} in various electrolytes (Figure 1c–f). When the BBI additive was introduced, the Zn deposition layer became more compact and uniform (Figure 1d–f). Furthermore, when the BBI additive concentration was over 0.25 g L^{-1}, the Zn deposition layer essentially achieved dendrite-free deposition behavior (Figure 1e,f). In addition, the X-ray diffraction (XRD) patterns showed that the relative intensities of the (002) ($I_{(002)}$) and (100) ($I_{(100)}$) peaks of different Zn deposition layers presented a significant increase with increasing BBI additive concentration (Figure 1g,h). Based on the hcp structure of Zn (Figure 1i), it can be inferred that the BBI additive might promote the Zn deposition along the (002) plane. In addition, the Zn deposition morphology in beaker cells was also observed. SEM images revealed a similar phenomenon (Figure S1a–h, Supporting Information). Taking into account that a compact and uniform Zn deposition behavior can be achieved when the additive concentration reaches 0.25 g L^{-1}, the electrolyte with a BBI additive concentration of 0.25 g L^{-1} was selected as the primary research object. Moreover, the real-time evolution of Zn deposition morphology in two electrolytes was also observed using an *in situ* optical microscope. In the $ZnSO_4$ electrolyte, a distinct black and non-uniform deposition layer appeared on the cross-section of Zn metal and became thicker over time (Figure S2a, Supporting Information). In contrast, in BBI/$ZnSO_4$ electrolyte, the cross-section of Zn metal exhibited a uniformly compact deposition feature, with almost no deposition layer observed (Figure S2b, Supporting Information). Polarization curve analysis was used to assess Zn metal corrosion in both electrolytes (Figure 1j). The corrosion potentials (E_{corr}s) and corrosion current densities (i_{corr}s) were determined using the intersection point of the anodic Tafel line. Both E_{corr}s were −0.993 V versus the saturated calomel electrode. However, i_{corr} in the BBI/$ZnSO_4$ electrolyte (1.483 mA cm^{-2}) was significantly lower than that in the $ZnSO_4$ electrolyte (3.459 mA cm^{-2}). Furthermore, the stability of Zn metal immersed in both electrolytes was investigated using XRD (Figure 1k) and SEM (Figure 1l–o). The results demonstrated that the BBI additive effectively inhibited the production of micrometer-sized by-products of $Zn_4SO_4(OH)_6{\cdot}xH_2O$.

To explore the modification mechanism of BBI additive, a series of experimental characterizations were conducted. The attenuated total reflection Fourier transform infrared (ATR-FTIR) spectra showed that regardless of whether the concentration of the BBI additive was 0.25 or 2.5 g L^{-1}, no significant shift was observed in the vibration stretching peak of ν-SO_4^{2-} ≈1081 cm^{-1} (**Figure 2**a). Likewise, the Raman spectra provided consistent results, showing no significant shifts in the vibration stretching peaks of Zn—O bonds in the range of 300–700 cm^{-1} or in ν-SO_4^{2-} at ≈981 cm^{-1} (Figure 2b). Furthermore, liquid-state nuclear magnetic resonance (NMR) analysis of different solutions indicated that the shift in the ^2H peak position was solely associated with the introduction of $ZnSO_4$ and free water, unrelated to the presence of the BBI additive (Figure 2c). Therefore, it can be reasonably inferred that the BBI additive cannot disrupt the electrostatic coupling between Zn^{2+} and SO_4^{2-}, indicating that the effect of the BBI additive on the solvation shell structure of Zn^{2+} can be ignored.[13] In addition, X-ray photoelectron spectroscopy (XPS) was further used to analyze the interaction between BBI anions and Zn metal. Specifically, for the original BBI, the C—C/C=C, —NH—, and —SO_2- groups were observed in the high-resolution spectra of C 1s, N 1s, and S 2p, respectively, with the weak C—O peak likely attributed to impurities (Figure 2d–f). By contrast, for the Zn metal after immersing in the BBI/$ZnSO_4$ electrolyte, a new peak appeared at ≈289 eV, which was assigned to the carbonates peak formed by the reaction between dissolved CO_2 in the electrolyte and Zn metal (Figure 2d).[14] In addition, a similar result was observed on Zn metal before immersion (Figure S3a, Supporting Information). Furthermore, a distinct N—Zn bond characteristic peak was observed at 399.6 eV, and the peak location was shifted from the peak location of the —NH_2 bond at 400.2 eV, suggesting the chemical bonding through N—Zn bond between the BBI additive and Zn metal (Figure 2e). In contrast, no significant nitrogen signal was observed on the Zn metal surface before immersion (Figure S3b, Supporting Information). Additionally, there was no significant difference between the S 2p spectra of BBI and BBI/Zn (Figure 2f). To further investigate the interfacial composition between Zn metal and BBI/$ZnSO_4$ electrolyte, transmission electron microscopy (TEM) analysis was carried out on the deposited Zn samples. Figure 2g corresponds to the schematic diagram of TEM sample preparation. As depicted in Figure 2h, distinct lattice fringes were observed, corresponding to the (002) crystal planes of the deposited Zn particles. Additionally, from the high-angle annular dark-field (HAADF) image (Figure 2i) and the corresponding elemental mapping presented in Figure 2j–n, it can be seen that the coexistence of C, N, O, S, and Zn elements, confirming the existence of BBI-Zn interfacial layer on the deposited Zn particles.

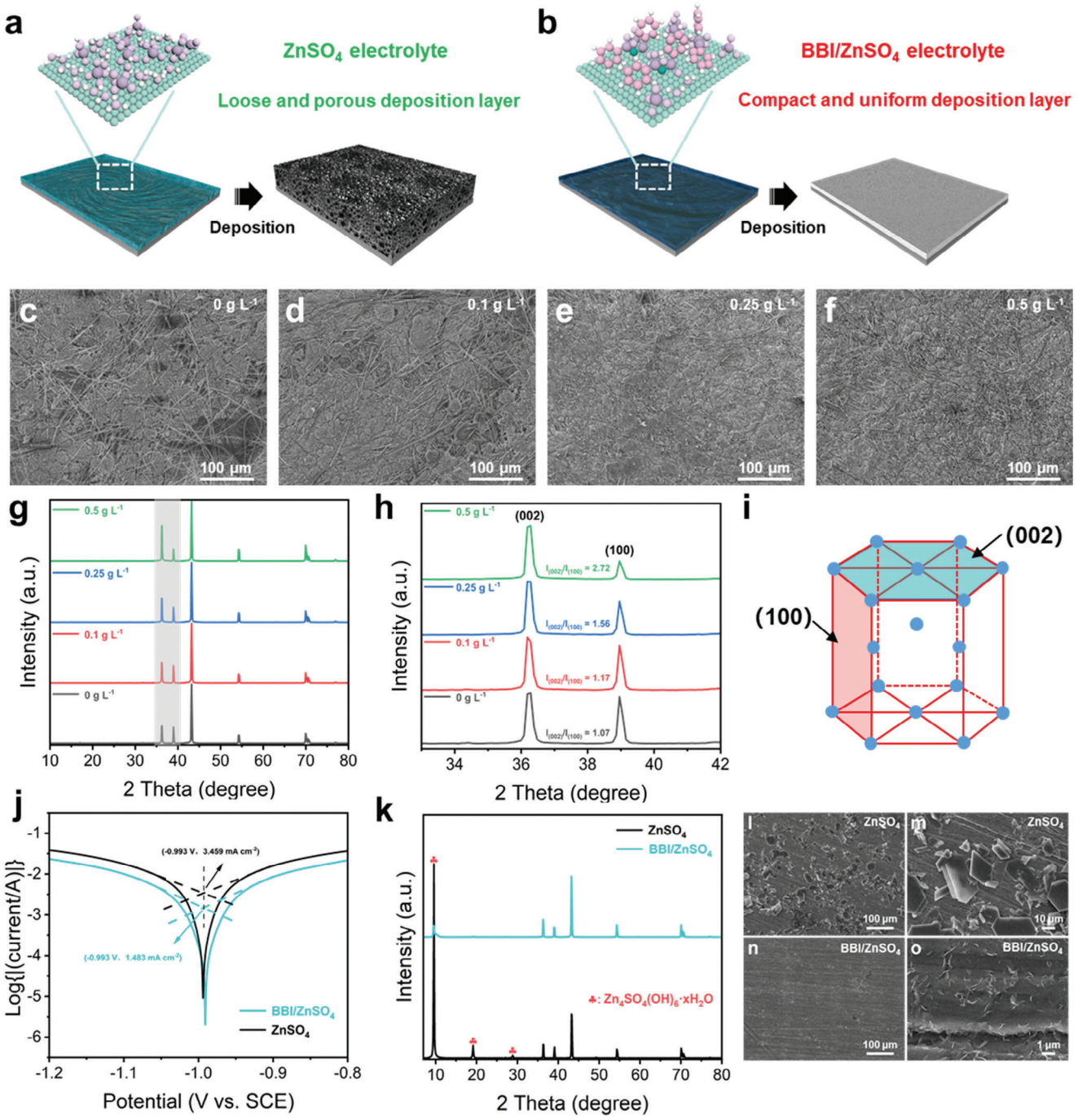

Figure 1. Effects of BBI additive on Zn deposition and corrosion resistance of Zn metal. a,b) Schematic illustration of Zn deposition behaviors in two electrolytes. c–f) SEM images of Zn deposition layers in BBI/$ZnSO_4$ electrolyte with different concentrations of BBI additives at 10 mA cm^{-2} and 5 mAh cm^{-2}. g,h) XRD patterns of Zn deposition layers. i) The crystal structure of Zn metal. j) Corrosion polarization curves of Zn metal in $ZnSO_4$ and BBI/$ZnSO_4$ electrolyte. k) The XRD patterns of Zn metal immersed in $ZnSO_4$ and BBI/$ZnSO_4$ electrolyte after seven days. l–o) Corresponding SEM images of immersed Zn metal.

To further investigate the effect of the BBI-Zn interfacial layer on the corrosion resistance of Zn metal, a series of computational studies and experimental characterizations were carried out. First, the pH measurements result revealed that the pH values gradually decreased as BBI concentration increased, suggesting the ionization of BBI leading to the formation of hydrogen ions (H^+) and BBI anions (Figure S4, Supporting Information). Figure S5 (Supporting Information) corresponds to the chemical formula of the BBI molecule. Subsequently, density functional theory calculations were conducted to investigate the adsorption

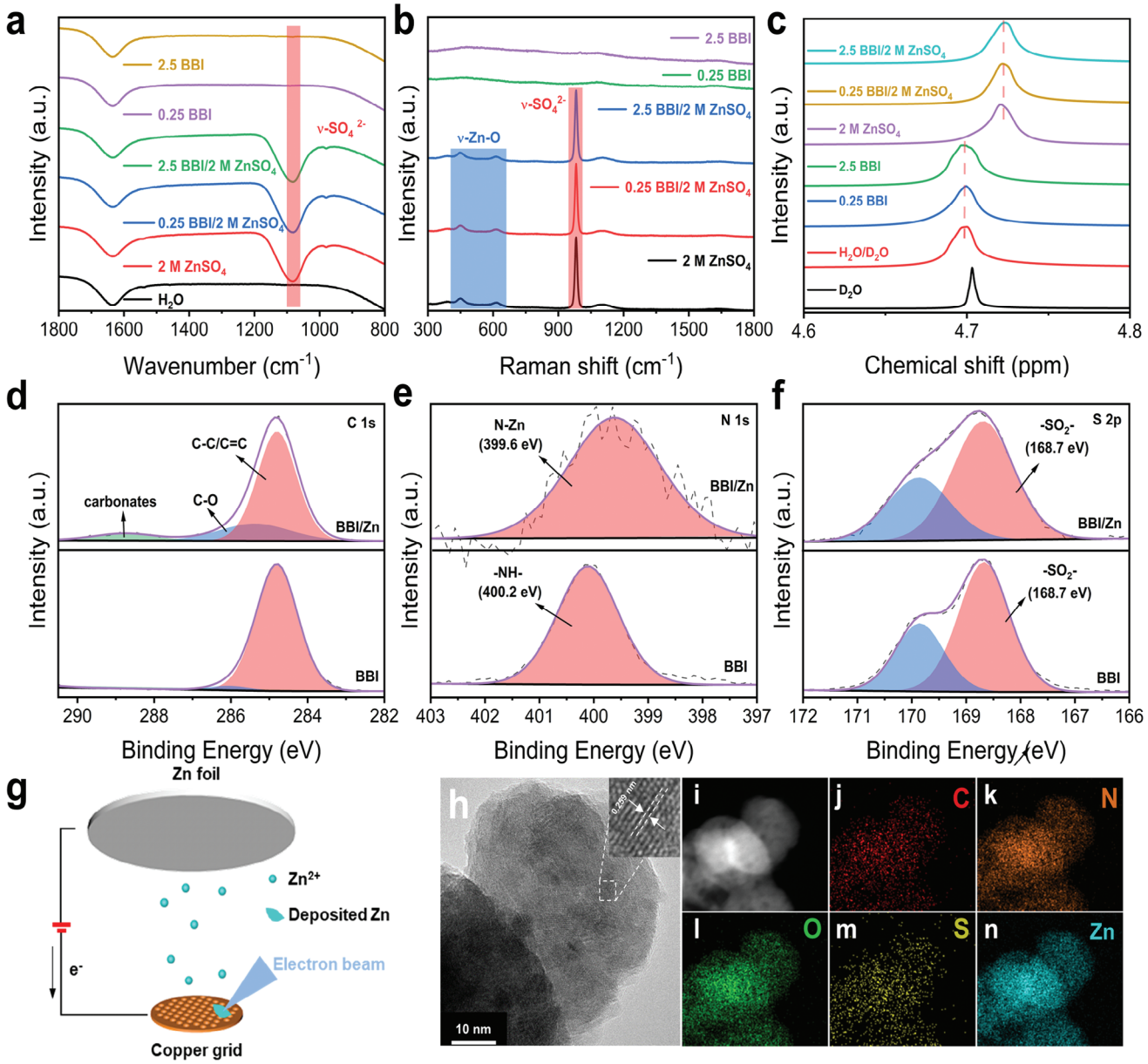

Figure 2. Modification mechanism of BBI additive. a) ATR-FTIR spectra, b) Raman spectra, and c) ^{2}H NMR spectra of various solutions. The High-resolution XPS spectra of BBI and BBI/Zn: d) C 1s; e) N 1s; f) S 2p. g) Schematic diagram of deposited Zn on the copper grid at 10 mA cm^{-2} in BBI/$ZnSO_4$ electrolyte. h) TEM image of deposited Zn sample. Corresponding i) HAADF image and j–n) elemental mapping images.

behavior. Geometric models were established to illustrate the adsorption of water, BBI molecule, and BBI anion on Zn metal, as presented in Figure S6a–d (Supporting Information). The adsorption energies of these species on the Zn (100) plane were calculated and found to be −0.641, −1.577, and −4.124 eV, respectively (**Figure 3a**). The BBI anions exhibited the lowest adsorption energy, indicating that they possessed the strongest interaction with Zn metal. Furthermore, the adsorption energy of the BBI anion on the Zn (002) plane was calculated to be −3.758 eV (Figure 3a). This result suggested a higher tendency for the BBI anion to be adsorbed on the Zn (100) plane rather than the (002) plane. The differential charge density diagram demonstrated significant charge transfer (CT) phenomena (Figure 3b). Quantitative calculations of charge distribution confirmed the presence of CT between the BBI anions and Zn metal. The BBI anions received 0.821 |e| from the Zn metal surface, confirming their chemical adsorption onto the surface of the Zn metal. In addition, the differential capacitance curves demonstrated that the incorporation of the BBI additive resulted in a decrease in the capacitance of the EDL. This reduction could be attributed to the chemical adsorption behavior of the BBI anions, which led to a depletion of surface water molecules. The larger size of the BBI molecule, compared to water molecules, induced the formation of a thicker inner Helmholtz layer, resulting in a decrease in EDL

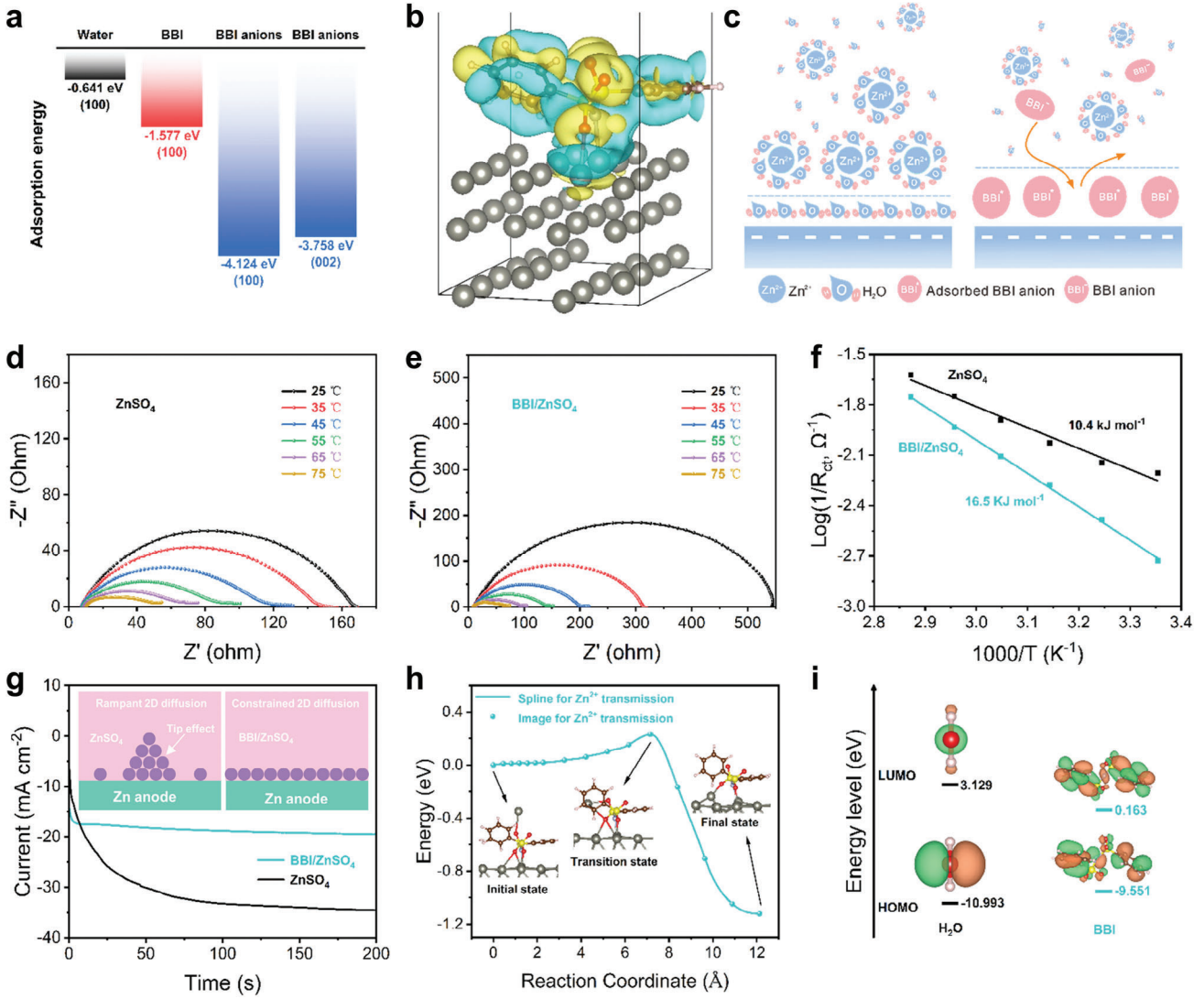

Figure 3. Regulatory mechanism of BBI-Zn interfacial layer. a) The adsorption energy of H_2O, BBI, and BBI anions on Zn metal surface. b) The charge density difference diagram of BBI anions adsorbed on the Zn metal surface. c) Schematic diagram of Zn metal surface EDL structure in two electrolytes (BBI^* represents the BBI anions chemically bonded with Zn surface). EIS of the Zn electrodes in the d) $ZnSO_4$ and e) $BBI/ZnSO_4$ electrolytes at different temperatures. f) The calculated de-solvation activation energies of both Zn electrodes in symmetric cells by using the Arrhenius equation. g) CA curves of Zn electrodes at a −150 mV overpotential. h) First-principles calculation of the Zn^{2+} migration energy barrier in the BBI-Zn interfacial layer. i) HOMO–LUMO energy levels of BBI and water molecules.

capacitance (Figure S7, Supporting Information).[15] Figure 3c illustrates the evolution of the EDL structure on the surface of Zn metal before and after the introduction of BBI. Specifically, when Zn metal was immersed in the $ZnSO_4$ electrolyte, the polarization effect of water molecules led to the formation of water-rich EDL on the surface of Zn metal, exacerbating side reactions such as HER and corrosion. However, upon the addition of BBI, the BBI anions replaced the polarized water molecules through their strong adsorption interaction with the Zn metal. This led to the conversion of water-rich EDL into water-poor EDL, inhibiting the undesirable side reactions.[12] Furthermore, the relationship between the open circuit potential value of the Zn electrode and immersing time in $BBI/ZnSO_4$ electrolyte with different additive concentrations was investigated (Figure S8, Supporting Information). The effect of BBI additive on the interfacial EDL potential can be described by the Nernst equation:

$$\varphi = \varphi_\theta + \frac{0.0592}{n} \log \frac{[oxidation\ type]}{[reduction\ type]} \quad (1)$$

where φ_θ represents the standard electrode potential, and n represents the number of electrons transferred. The [oxidation type]/[reduction type] ratio represents the product of the concentration of all reactants divided by the product of the concentration of the reaction products. The concentration exponents should be equal to the coefficients of the reactants in the electrode reaction.[16] H^+ ions belong to the oxidation type, while Zn^{2+}

ions belong to the reduction type. Therefore, introducing BBI resulted in a positive shift in interfacial potential. When BBI was absent, the interfacial potential decreased negatively over time due to continuous HER. However, with BBI present, the interfacial potential initially decreased, and then stabilized or slightly increased. This could be attributed to the chemical adsorption of BBI anions on Zn metal, which effectively hinders the continuous HER. However, if the amount of BBI added was too high, the interfacial potential continued to decrease negatively, which could be likely due to low pH causing vigorous HER, which hindered the stable formation of the BBI-Zn interfacial layer.

In addition, to understand the modification mechanism of BBI-Zn interfacial layer on Zn deposition behavior, a series of experiments were carried out. Cyclic voltammetry (CV) results showed that the BBI-Zn interfacial layer led to an increase in Zn nucleation overpotential (Figure S9, Supporting Information).[17] Moreover, the morphology of Zn deposition layers and deposition curves while keeping the capacity constant but varying either the current density or BBI additive concentration also are explored. The results confirmed that as the current density or additive concentration increased, the nucleation overpotential of Zn^{2+} also increased, leading to the gradual densification of the Zn deposition layer (Figures S10a–f and S11a—f, Supporting Information), conforming to classical nucleation and growth theory.[17b] Additionally, an in-depth examination of the de-solvation process of Zn^{2+} using variable-temperature Electrochemical Impedance Spectroscopy (EIS) was conducted. The Arrhenius equation was employed to elucidate the process of de-solvation of Zn^{2+} in terms of activation energy (E_a), as depicted below:

$$1/R_{ct} = \mathrm{Aexp}\left(-E_a/(\mathrm{R} * \mathrm{T})\right) \quad (2)$$

where R_{ct} represents the interface resistance, A is the frequency factor, R stands for the gas constant, and T denotes the absolute temperature.[18] Figure 3d,e showed that the Zn electrode exhibited markedly elevated charge transfer impedance in the BBI/$ZnSO_4$ electrolyte at various temperatures ranging from 25 to 75 °C. The E_a for the Zn electrode in the BBI/$ZnSO_4$ electrolyte was ≈16.5 kJ mol^{-1}, which exceeded that in the $ZnSO_4$ electrolyte (10.4 kJ mol^{-1}) (Figure 3f). This heightened activation energy indicated that the de-solvation process of Zn^{2+} was impeded, resulting in substantial polarization and an escalation in nucleation overpotential. To further examine the impact of two electrolytes on the deposition behavior of Zn, a chronoamperometry (CA) test was performed at a fixed voltage of -150 mV (Figure 3g). In the $ZnSO_4$ electrolyte, the current-time curve of the Zn electrode presented a typical mechanism of nucleation growth dominated by unrestricted 2D diffusion, and the current density increased with time, which easily led to the formation of dendrites. In contrast, the current-time curve of the Zn electrode in BBI/$ZnSO_4$ electrolyte showed a mechanism of nucleation growth dominated by 3D diffusion, and the current density remained stable after the first few seconds, which was conducive to obtaining compact and uniform Zn deposition layer.[19] In addition, the analysis of the Zn^{2+} transport process within the BBI-Zn interfacial layer was conducted. As depicted in Figure S12 (Supporting Information), a distinctive diffusion channel for Zn^{2+} along the c-axis in the BBI-Zn interfacial layer was identified. The migration energy barrier for Zn^{2+} diffusion along this pathway was calculated to be 0.232 eV (Figure 3h), indicating that the migration process of Zn^{2+} was notably hindered. Therefore, it can be reasonably deduced that the affinity of BBI anion for adsorption on the Zn (100) plane resulted in the suppression of Zn^{2+} deposition along the Zn (100) plane, while consequently enhancing the deposition of Zn^{2+} along the Zn (002) plane.[20] In addition, the surface composition and morphology of the cycled Zn electrodes were also analyzed. In the BBI/$ZnSO_4$ electrolyte, the surface of Zn metal exhibited a flat and compact morphology (Figure S13a, Supporting Information), while in the $ZnSO_4$ electrolyte, the surface of Zn metal presented a loose and porous dendrite morphology (Figure S13b, Supporting Information). Furthermore, the cross-sectional SEM images demonstrated that in the BBI/$ZnSO_4$ electrolyte (Figure S13c, Supporting Information), Zn metal exhibited a thin and compact deposition layer, whereas in the $ZnSO_4$ electrolyte (Figure S13d, Supporting Information), Zn metal displayed a thick and loose deposition layer. Moreover, XPS analysis was conducted to investigate the surface composition of Zn metal after cycling in BBI/$ZnSO_4$ electrolyte. As illustrated in Figure S14 (Supporting Information), the chemical-bonded BBI-Zn interfacial layer or its derivatives was detected on the surface without Ar^+ sputtering. The peak of ZnS should be attributed to the decomposition of the BBI-Zn interfacial layer. In addition, as the Ar^+ sputtering time increased, the peak intensity of ZnS became gradually stronger. Considering that the decomposition of the BBI-Zn interfacial layer required the involvement of H^+, it could be understood as when electrons were accumulating on the Zn anode surface, BBI anions first combined with H^+ to form tightly adsorbed BBI molecules. Therefore, molecular orbital level calculations were performed for water molecules and BBI molecules (Figure 3i). In comparison to the water molecule, BBI displayed a higher highest occupied molecular orbital (HOMO) (−9.551 eV vs −10.993 eV) and a lower lowest unoccupied molecular orbital (LUMO) (0.163 eV vs 3.129 eV). Consequently, BBI exhibited a greater inclination to accept electrons, thereby facilitating its reduction and transformation into a SEI.[11]

To provide further demonstration of the interfacial regulatory mechanism of BBI, a comprehensive evaluation of electrochemical performance was conducted on a series of symmetric and asymmetric cells. Initially, Zn paired with copper (Cu) asymmetric cells were used to determine the coulombic efficiency (CE) at 10 mA cm^{-2} and a capacity of 5 mAh cm^{-2}, allowing us to investigate the reversibility of Zn^{2+} deposition/dissolution (**Figure 4a**). In the BBI/$ZnSO_4$ electrolyte, the Zn electrode exhibited high coulomb efficiency (CE) over 600 cycles with an average CE value of up to 99.8%, whereas in the $ZnSO_4$ electrolyte, electrode failure occurred after <100 cycles. Additionally, the Zn electrode in BBI/$ZnSO_4$ electrolyte exhibited a higher voltage hysteresis (136 mV) compared to the $ZnSO_4$ electrolyte (97 mV) (Figure 4b,c). In addition, Figure S15 (Supporting Information) showed the optical photographs of Zn deposition layers on Cu electrodes with different deposition areal specific capacities in two electrolytes. In the $ZnSO_4$ electrolyte, the Zn deposition layers appeared black due to their porous and loose structure that prevented light reflection, whereas, in the BBI/$ZnSO_4$ electrolyte, the Zn deposition layers appeared white owing to their compact structure that absorbed little light. Furthermore, the rate capabilities of the Zn electrodes were examined under different current densities (10, 20, 30, 40, and 50 mA cm^{-2}),

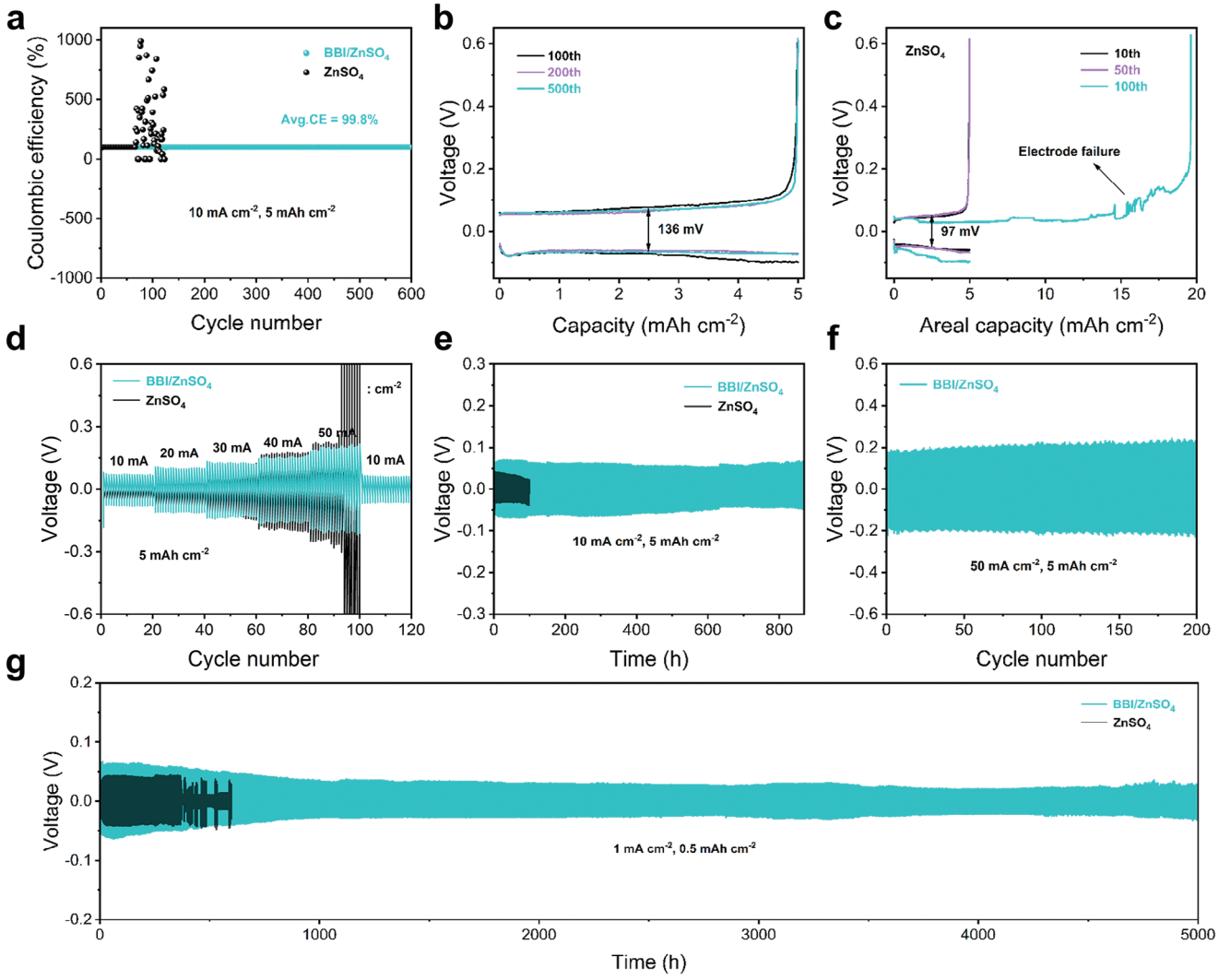

Figure 4. Electrochemical performance of Zn||Cu and Zn||Zn cells. a) CE of Zn deposition/dissolution on Cu and b,c) the corresponding voltage profiles. d) Rate capabilities of Zn||Zn cells under different current densities of 10, 20, 30, 40, and 50 mA cm^{-2} and a constant capacity of 5 mAh cm^{-2}. Galvanostatic cycling performance of Zn||Zn cells at e) 10 mA cm^{-2}/5 mAh cm^{-2} and f) 50 mA cm^{-2}/5 mAh cm^{-2}. g) Long-term galvanostatic cycling performance of Zn||Zn cells at 1 mA cm^{-2}/0.5 mAh cm^{-2}.

with a constant capacity of 5 mAh cm^{-2} (Figure 4d). The Zn electrode in the BBI/$ZnSO_4$ electrolyte still delivered stable deposition/dissolution curves even at 50 mA cm^{-2}, while the Zn electrode in the $ZnSO_4$ electrolyte failed to operate effectively. In addition, the cyclic stability tests on Zn electrodes were carried out in two electrolytes under 10 mA cm^{-2} and a capacity of 5 mAh cm^{-2} (Figure 4e). The Zn electrode in the BBI/$ZnSO_4$ electrolyte exhibited a significantly extended cycling life, surpassing 800 h, compared to the Zn electrode in the $ZnSO_4$ electrolyte. The electrochemical performance tests were also carried out on Zn electrodes using other concentrations of BBI/$ZnSO_4$ electrolyte (Figure S16a,b, Supporting Information). Furthermore, we conducted tests to evaluate the ionic conductivity of various concentrations of BBI/$ZnSO_4$ electrolyte. The results revealed that the ionic conductivity remained consistent across different additive concentrations, which suggested that the voltage hysteresis was solely attributable to the chemical adsorption layer of the additive (Figure S17, Supporting Information). In addition, the Zn||Zn symmetric cell can keep stable cycling up to 200 cycles in the BBI/$ZnSO_4$ electrolyte even under the highly demanding test conditions of 50 mA cm^{-2} and a capacity of 5 mAh cm^{-2} (Figure 4f). Moreover, the Zn electrode exhibited an exceptional cycling life of up to 5000 h at 1 mA cm^{-2} in the BBI/$ZnSO_4$ electrolyte, surpassing the cycling life of the Zn electrode in the $ZnSO_4$ electrolyte. In addition, the EIS test after cycling showed a small charge transfer impedance (Figure S18, Supporting Information), which corresponded to the phenomenon that the voltage hysteresis gradually decreased during cycling (Figure 4g). This could be attributed to the high Zn^{2+} conductivity of the rich ZnS phase SEI layer derived from the BBI-Zn interfacial layer during cycling.[14c]

Considering the excellent cycling life of interfacial regulated Zn electrode by BBI additive, the activated carbon (AC) as the cathode material was selected to assemble AZICs. First, the rate

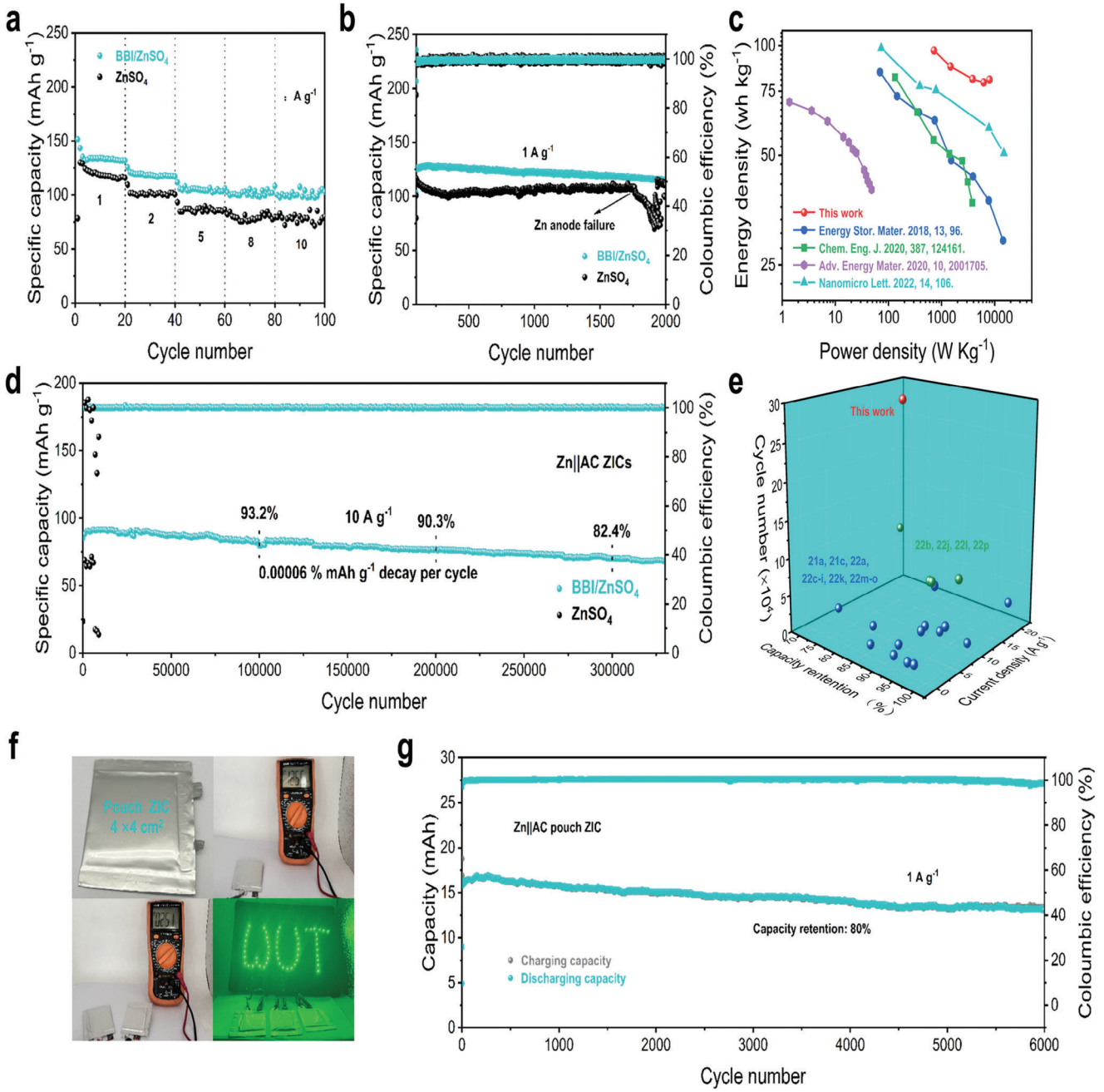

Figure 5. Electrochemical performance of Zn||AC ZICs. a) Rate capabilities at different current densities. b) Long-term cycling stability and efficiency after rate test at 1 A g^{-1}. c) Ragone plot comparing with other AZICs reported. d) Cyclic stability test at 10 A g^{-1}. e) Comparison of cycling life with previous reports. f) Digital photographs of pouch AZICs. g) Cycling stability test of pouch AZIC in BBI/$ZnSO_4$ at 1 A g^{-1}.

performance of AZICs in two electrolytes under various current densities was evaluated and they both demonstrated good rate performance (**Figure** 5a). Notably, the AZIC in BBI/$ZnSO_4$ electrolyte exhibited a higher capacity, which may be attributed to BBI suppressing the side reactions. The charge-discharge curves at different current densities also showed low polarization (Figure S19, Supporting Information). Additionally, the reaction kinetics of the AZIC in BBI/$ZnSO_4$ electrolyte was further analyzed using multi-scan rate CV. A typical pseudocapacitive energy storage mechanism was revealed, explaining the reason for its excellent rate performance (Figure S20a–d, Supporting Information). In addition, at 1 A g^{-1}, the AZIC in BBI/$ZnSO_4$ electrolyte can maintain good cycling stability during 2000 cycles, while the electrode failure occurred at ≈1760 cycles for that in $ZnSO_4$ electrolyte (Figure 5b). Additionally, the energy density and power density of AZIC in BBI/$ZnSO_4$ electrolytes were compared with those reported in recent literature, demonstrating a significant advantage (Figure 5c).[21] The long-term cycling performance of

two AZICs at 10 A g^{-1} was also evaluated. The AZIC in $ZnSO_4$ electrolyte cannot continue cycling after <10 000 cycles due to electrode failure, while the AZIC in BBI/$ZnSO_4$ electrolyte exhibited remarkable long-term cycling stability, with a cycling life exceeding 300 000 cycles and lasting over six months. The capacity retention rates were 93.2%, 90.3%, and 82.4% for 100 000, 200 000, and 300 000 cycles, respectively. Additionally, the attenuation rate of the single-cycle capacity was 0.00006% (Figure 5d). In addition, the SEM images of the Zn metal electrodes after cycling showed that the surface of the Zn foil remained smooth and compact after 100 000 cycles in the BBI/$ZnSO_4$ electrolyte (Figure S21a, Supporting Information). In contrast, large holes appeared on the surface of the Zn foil after only 10 000 cycles in the $ZnSO_4$ electrolyte, and a large amount of glass fibers were embedded in the Zn metal (Figure S21b, Supporting Information). Similar phenomena were observed in the cross-sectional SEM images. In BBI/$ZnSO_4$ electrolyte, the active Zn was still sufficient after 100 000 cycles (Figure S21c, Supporting Information). However, in the $ZnSO_4$ electrolyte, the active Zn was even completely deactivated after only 10 000 cycles (Figure S21d, Supporting Information). It can be reasonably speculated that repeated high-current density cycling in $ZnSO_4$ electrolyte led to a continuous reduction of active Zn due to dendrite growth and side reactions, resulting in the Zn metal anode gradually becoming porous or even fracturing, ultimately leading to complete electrode failure. Compared to AZICs with long cycling performance reported in recent years, the assembled AZIC based on the BBI additive interfacial regulation mechanism exhibited the longest cycling life (Figure 5e).[21a,c,22] In addition, the pouch AZICs were also assembled based on BBI/$ZnSO_4$ electrolyte, with an open circuit voltage of 1.255 V for a single AZIC, and 2.51 V for the two AZICs connected in parallel, demonstrating good consistency (Figure 5f). Moreover, three AZICs connected in parallel can easily light up a lamp (Figure 5f). Most importantly, the assembled pouch AZIC can maintain 80% of the capacity retention even after 6000 cycles at 1 A g^{-1}, indicating significant potential for practical applications (Figure 5g).

3. Conclusion

In conclusion, an interface engineering strategy using BBI additive had been employed to achieve AZICs with an ultra-long cycling life. This was mainly attributed to the formation of the BBI-Zn interfacial layer through the BBI anions chemical bonding on Zn metal, which converted the original water-rich EDL into a water-poor EDL, thus efficiently suppressing HER and corrosion reactions. Furthermore, this interfacial layer slowed down the deposition process of Zn^{2+} and increased the nucleation overpotential of Zn^{2+}, ultimately achieving compact Zn deposition behavior. In addition, the SEI layer derived from this interfacial layer further regulated the diffusion of Zn^{2+}. Based on the additive interface engineering strategy, Zn||Zn symmetric and Zn||Cu asymmetric cells achieved over 800 h of cycling life and 99.8% of high average CE at 10 mA cm^{-2}, respectively. Moreover, excellent rate performance of up to 50 mA cm^{-2} had been achieved in BBI/$ZnSO_4$ electrolyte. In addition, a cycling life of 5000 h was demonstrated at 1 mA cm^{-2}, exhibiting superior cycling stability. Even more encouragingly, the assembled Zn||AC AZIC in BBI/$ZnSO_4$ electrolyte achieved a cycling life of over 300 000 cycles and a duration of over 6 months. The assembled pouch AZIC can maintain 80% capacity retention after 6000 cycles, demonstrating its enormous potential for large-scale applications.

Supporting Information

Supporting Information is available from the Wiley Online Library or from the author.

Acknowledgements

W.S. and Z.S. contributed equally to this work. This work was supported by the National Natural Science Foundation of China (52072285, 52172231, and 51972259) and the Natural Science Foundation of Hubei Province (2022CFA087).

Conflict of Interest

The authors declare no conflict of interest.

Data Availability Statement

The data that support the findings of this study are available from the corresponding author upon reasonable request.

Keywords

aqueous zinc ion capacitors, cycling life, electric double layer, electrode/electrolyte interface, interface engineering

Received: September 25, 2023
Revised: October 28, 2023
Published online: November 21, 2023

[1] a) T. M. Gür, *Energy Environ. Sci.* **2018**, *11*, 2696; b) X. Wang, M. Salari, D.-E. Jiang, J. Chapman Varela, B. Anasori, D. J. Wesolowski, S. Dai, M. W. Grinstaff, Y. Gogotsi, *Nat. Rev. Mater.* **2020**, *5*, 787; c) C. Choi, D. S. Ashby, D. M. Butts, R. H. Deblock, Q. Wei, J. Lau, B. Dunn, *Nat. Rev. Mater.* **2019**, *5*, 5; d) Z. Li, S. Gadipelli, H. Li, C. A. Howard, D. J. L. Brett, P. R. Shearing, Z. Guo, I. P. Parkin, F. Li, *Nat. Energy* **2020**, *5*, 160; e) F. Cheng, J. Liang, Z. Tao, J. Chen, *Adv. Mater.* **2011**, *23*, 1695.
[2] B. Zakeri, S. Syri, *Renew. Sust. Energ. Rev.* **2015**, *42*, 569.
[3] a) L. Dong, W. Yang, W. Yang, Y. Li, W. Wu, G. Wang, *J. Mater. Chem. A* **2019**, *7*, 13810; b) H. Wang, W. Ye, Y. Yang, Y. Zhong, Y. Hu, *Nano Energy* **2021**, *85*, 105942; c) H. Tang, J. Yao, Y. Zhu, *Adv. Energy Mater.* **2021**, *11*, 2003994; d) K. Qu, X. Lu, Z. Huang, J. Liu, *Mater. Today Energy* **2022**, *30*, 101188.
[4] a) C. Li, X. Xie, S. Liang, J. Zhou, *Energy Environ. Sci.* **2020**, *3*, 146; b) Z. Yi, G. Chen, F. Hou, L. Wang, J. Liang, *Adv. Energy Mater.* **2020**, *11*, 2003065.
[5] C. Lin, X. Yang, P. Xiong, H. Lin, L. He, Q. Yao, M. Wei, Q. Qian, Q. Chen, L. Zeng, *Adv. Sci.* **2022**, *9*, 2201433.
[6] W. Du, E. H. Ang, Y. Yang, Y. Zhang, M. Ye, C. C. Li, *Energy Environ. Sci.* **2020**, *13*, 3330.
[7] Y. Su, B. Liu, Q. Zhang, J. Peng, C. Wei, S. Li, W. Li, Z. Xue, X. Yang, J. Sun, *Adv. Funct. Mater.* **2022**, *32*, 2204306.
[8] Y. Zhu, J. Yin, X. Zheng, A.-H. Emwas, Y. Lei, O. F. Mohammed, Y. Cui, H. N. Alshareef, *Energy Environ. Sci.* **2021**, *14*, 4463.

[9] J. Cao, D. Zhang, C. Gu, X. Wang, S. Wang, X. Zhang, J. Qin, Z.-S. Wu, *Adv. Energy Mater.* **2021**, *11*, 2101299.
[10] Y. Du, Y. Li, B. B. Xu, T. X. Liu, X. Liu, F. Ma, X. Gu, C. Lai, *Small* **2022**, *18*, 2104640.
[11] Y. Liu, Y. An, L. Wu, J. Sun, F. Xiong, H. Tang, S. Chen, Y. Guo, L. Zhang, Q. An, L. Mai, *ACS Nano* **2023**, *17*, 552.
[12] C. Huang, X. Zhao, S. Liu, Y. Hao, Q. Tang, A. Hu, Z. Liu, X. Chen, *Adv. Mater.* **2021**, *33*, 2100445.
[13] a) H. Yang, Z. Chang, Y. Qiao, H. Deng, X. Mu, P. He, H. Zhou, *Angew. Chem., Int. Ed.* **2020**, *59*, 9377; b) Z. Hu, F. Zhang, Y. Zhao, H. Wang, Y. Huang, F. Wu, R. Chen, L. Li, *Adv. Mater.* **2022**, *34*, 2203104.
[14] a) Y.-X. Song, J. Wang, X.-B. Zhong, K. Wang, Y.-H. Zhang, H.-T. Liu, L.-X. Zhang, J.-F. Liang, R. Wen, *Energy Stor. Mater.* **2023**, *58*, 85; b) H. Qiu, X. Du, J. Zhao, Y. Wang, J. Ju, Z. Chen, Z. Hu, D. Yan, X. Zhou, G. Cui, *Nat. Commun.* **2019**, *10*, 5374; c) J. Hao, B. Li, X. Li, X. Zeng, S. Zhang, F. Yang, S. Liu, D. Li, C. Wu, Z. Guo, *Adv. Mater.* **2020**, *32*, 2003021.
[15] K. Wang, F. Liu, Q. Li, J. Zhu, T. Qiu, X.-X. Liu, X. Sun, *Chem. Eng. J.* **2023**, *452*, 139577.
[16] K. W. Knehr, E. C. Kumbur, *Electrochem. Commun.* **2011**, *13*, 342.
[17] a) W. Yang, X. Du, J. Zhao, Z. Chen, J. Li, J. Xie, Y. Zhang, Z. Cui, Q. Kong, Z. Zhao, C. Wang, Q. Zhang, G. Cui, *Joule* **2020**, *4*, 1557; b) A. Pei, G. Zheng, F. Shi, Y. Li, Y. Cui, *Nano Lett.* **2017**, *17*, 1132.
[18] Y. Yang, C. Liu, Z. Lv, H. Yang, Y. Zhang, M. Ye, L. Chen, J. Zhao, C. C. Li, *Adv. Mater.* **2021**, *33*, 2007388.
[19] Z. Zhao, J. Zhao, Z. Hu, J. Li, J. Li, Y. Zhang, C. Wang, G. Cui, *Energy Environ. Sci.* **2019**, *12*, 1938.
[20] H. Zhang, Y. Zhong, J. Li, Y. Liao, J. Zeng, Y. Shen, L. Yuan, Z. Li, Y. Huang, *Adv. Energy Mater.* **2022**, *13*, 2203254.
[21] a) L. Dong, X. Ma, Y. Li, L. Zhao, W. Liu, J. Cheng, C. Xu, B. Li, Q.-H. Yang, F. Kang, *Energy Stor. Mater.* **2018**, *13*, 96; b) H. He, J. Lian, C. Chen, Q. Xiong, C. c. Li, M. Zhang, *Nanomicro Lett* **2022**, *14*, 106; c) J. Yin, W. Zhang, W. Wang, N. A. Alhebshi, N. Salah, H. N. Alshareef, *Adv. Energy Mater.* **2020**, *10*, 2001705; d) Y. Zheng, W. Zhao, D. Jia, Y. Liu, L. Cui, D. Wei, R. Zheng, J. Liu, *Chem. Eng. J.* **2020**, *387*, 124161.
[22] a) G.-H. An, J. Hong, S. Pak, Y. Cho, S. Lee, B. Hou, S. Cha, *Adv. Energy Mater.* **2019**, *10*, 1902981; b) Q. Fu, S. Hao, L. Meng, F. Xu, J. Yang, *ACS Nano* **2021**, *15*, 18469; c) L. Jin, X. Guo, R. Gong, J. Zheng, Z. Xiang, C. Zhang, J. P. Zheng, *Energy Stor. Mater.* **2019**, *23*, 409; d) X. Li, M. Li, Q. Yang, D. Wang, L. Ma, G. Liang, Z. Huang, B. Dong, Q. Huang, C. Zhi, *Adv. Energy Mater.* **2020**, *10*, 2001394; e) Z. Li, D. Chen, Y. An, C. Chen, L. Wu, Z. Chen, Y. Sun, X. Zhang, *Energy Stor. Mater.* **2020**, *28*, 307; f) P. Liu, W. Liu, Y. Huang, P. Li, J. Yan, K. Liu, *Energy Stor. Mater.* **2020**, *25*, 858; g) J. Luo, L. Xu, H. Liu, Y. Wang, Q. Wang, Y. Shao, M. Wang, D. Yang, S. Li, L. Zhang, Z. Xia, T. Cheng, Y. Shao, *Adv. Funct. Mater.* **2022**, *32*, 2112151; h) M. Peng, L. Wang, L. Li, X. Tang, B. Huang, T. Hu, K. Yuan, Y. Chen, *Adv. Funct. Mater.* **2021**, *32*, 2109524; i) Q. Fu, S. Hao, X. Zhang, H. Zhao, F. Xu, J. Yang, *Energy Environ. Sci.* **2023**, *16*, 1291; j) C. Wang, Z. Pei, Q. Meng, C. Zhang, X. Sui, Z. Yuan, S. Wang, Y. Chen, *Angew. Chem., Int. Ed.* **2021**, *60*, 990; k) H. Wang, M. Wang, Y. Tang, *Energy Stor. Mater.* **2018**, *13*, 1; l) L. Wang, M. Peng, J. Chen, T. Hu, K. Yuan, Y. Chen, *Adv. Mater.* **2022**, *34*, 2203744; m) Z. Wang, J. Huang, Z. Guo, X. Dong, Y. Liu, Y. Wang, Y. Xia, *Joule* **2019**, *3*, 1289; n) S. Wu, Y. Chen, T. Jiao, J. Zhou, J. Cheng, B. Liu, S. Yang, K. Zhang, W. Zhang, *Adv. Energy Mater.* **2019**, *9*, 1902915; o) R. Yuksel, O. Buyukcakir, P. K. Panda, S. H. Lee, Y. Jiang, D. Singh, S. Hansen, R. Adelung, Y. K. Mishra, R. Ahuja, R. S. Ruoff, *Adv. Funct. Mater.* **2020**, *30*, 1909725; p) H. Zhang, Q. Liu, Y. Fang, C. Teng, X. Liu, P. Fang, Y. Tong, X. Lu, *Adv. Mater.* **2019**, *31*, 1904948.